V European Conference on Computational Fluid Dynamics
ECCOMAS CFD 2010
J. C. F. Pereira and A. Sequeira (Eds)
Lisbon, Portugal,14-17 June 2010

# ABSORBING BOUNDARY CONDITIONS FOR WAVE SIMULATIONS AROUND OFFSHORE STRUCTURES

**Roel Luppes*, Arthur E.P. Veldman**, Peter R. Wellens†**

*University of Groningen, Institute of Mathematics and Computing Science,
PO Box 407, 9700 AK Groningen, The Netherlands
e-mail: {r.luppes,a.e.p.veldman}@rug.nl
†Deltares
PO Box 177, 2600 MH Delft, The Netherlands
e-mail: peter.wellens@deltares.nl

**Key words:** ComFLOW, VOF, Waves, Absorbing BC, Density Averaging

**Abstract.** *The CFD simulation tool ComFLOW, developed for the simulation of sloshing liquids and two-phase flow, is applied to study water waves around a semi-submersible model. ComFLOW solves the Navier-Stokes equations in both water and compressible air, with second order accuracy in both space and time. The water surface is advected by means of a modified Volume-of-Fluid (VOF) method, with improved accuracy through a height-function approach. Particular attention has been paid to the numerical treatment of the density around the interface. With a so-called 'gravity-consistent' density averaging method, severe instabilities near the free surface can be avoided.*
*An Absorbing Boundary Condition (ABC) has been developed for wave simulations in open domains, based on a rational function approximation of the linear dispersion relation for waves. This approximation is combined with the traditional Sommerfeld outflow condition, making use of an estimate of the local wave number. By employing the ABC at an outflow boundary, this boundary can be located relatively close to the object, without influencing outgoing waves or generating numerical reflections that affect the water wave inside the flow domain. When a traditional numerical beach or damping zone is used, this boundary has to be located very far behind the obstacle to avoid reflections. An important advantage of the ABC approach is therefore the smaller number of grid-points required for the same (or even higher) accuracy, which reduces the computing time considerably.*
*Simulations of waves around and wave run-up against a semi-submersible model are compared with measurements. The overall agreement is quite well, for a wide range of wave conditions. The ABC performs well, as numerical reflections are almost absent, even when the inflow and outflow boundaries are quite close to the model. Moreover, the computing times reduce with at least a factor four compared to other damping zone techniques.*

## 1 INTRODUCTION

During the life time of an offshore structure, it encounters a variety of loading conditions. Obviously, severe damage as a result of extreme wave loading needs to be prevented. With numerical simulations of the structure in waves, critical loading conditions can be indicated. In this way, simulations serve as an important engineering design tool.

The numerical method ComFLOW has been developed for the simulation of sloshing liquids and waves in e.g. offshore applications. It is based on the Navier-Stokes equations, in which a volume-of-fluid (VOF) method is applied to describe the evolution of the free surface[1–18]. ComFLOW intends to simulate extreme wave impact events, as if the structure were out at sea. For an accurate wave representation near the structure, spurious wave reflections from the domain boundaries should be prevented. A common approach is to incorporate numerical damping zones, which require multiple wave lengths to effectively dissipate wave energy and thus prevent reflections. However, this requirement conflicts with the desire to keep the domain confined to the direct surroundings of the structure, especially in case of long waves. Therefore, an absorbing boundary condition (ABC) has been developed for the benefit of extreme wave impact simulations with ComFLOW.

The derivation of the ABC is adopted from[18]. In this paper, more details on the incorporation in the numerical method are given. The ABC is tested in actual simulations and compared to theoretical reflection coefficients and to the performance of a traditional absorbing layer. Finally, the ABC is used in 3D simulations of waves around a semi-submersible, of which the outcome is validated with experimental results.

## 2 GOVERNING EQUATIONS

Since the cushioning effect due to the compressibility of air is important in wave impact simulations, the governing equations for compressible flow are given in conservation form (volume $\Omega$, boundary $\Gamma$, normal $\vec{n}$). In terms of time $t$, velocity $\vec{u}=(u,v,w)^T$, pressure $p$ and fluid density $\rho$ and viscosity $\mu$, conservation of mass and momentum are given by

$$\int_\Omega \frac{\partial \rho}{\partial t}\, d\Omega + \oint_\Gamma (\rho \vec{u}) \cdot \vec{n}\, d\Gamma = 0 \tag{1}$$

$$\int_\Omega \frac{\partial (\rho \vec{u})}{\partial t} d\Omega + \oint_\Gamma \rho \vec{u}\, (\vec{u} \cdot \vec{n})\; d\Gamma + \oint_\Gamma p\, \vec{n}\, d\Gamma - \oint_\Gamma \left( \mu \left( \nabla \vec{u} + \nabla \vec{u}^T \right) - \frac{2}{3}\, \mu \nabla \cdot \vec{u} \right) \cdot \vec{n}\, d\Gamma - \int_\Omega \rho \vec{F}\, d\Omega = 0. \tag{2}$$

In absence of further external loading, the external force $\vec{F}$ consists of gravity only. To include compressibility of air, the Navier-Stokes equations (1) and (2) are closed with an equation of state[12–18]

$$\frac{\rho_g}{\rho_{g,0}} = \left( \frac{p_g}{p_{g,0}} \right)^{1/\gamma}, \tag{3}$$

where $p_{g,0}$ and $\rho_{g,0}$ denote the constant atmospheric pressure and ambient gas density, respectively. The coefficient $\gamma = 1.4$ for pure air.

A no-slip boundary condition $\vec{u} = 0$ is imposed on the surface of the offshore structure. The same boundary condition is used for the domain bottom and ceiling, as well as the side walls, which is in accordance with the experimental setup described below. Hence, in the present study, ABCs are only used for the inflow and outflow boundaries.

The free surface is described by $F_s(\vec{x}, t) = 0$, and its motion is given by

$$\frac{DF_s}{Dt} = \frac{\partial F_s}{\partial t} + \vec{u} \cdot \nabla F_s = 0 \tag{4}$$

A force balance in terms of surface tension $\sigma$ and mean curvature $\kappa$ determines the boundary conditions at the interface in case of one-phase flow[1–11] or an additional body force in case of two-phase flow[12–18].

## 3 NUMERICAL METHOD

The numerical method ComFLOW is based on the Navier-Stokes equations, in which a volume-of-fluid (VOF) method is applied to describe the evolution of the free surface. In VOF methods, filling rates of individual cells are administrated. Fluid fragments are advected with local velocities and the free surface position is subsequently reconstructed from combined fluid volumes contained in single cells. ComFLOW has been developed initially at the University of Groningen to study the sloshing of liquid on board spacecraft in micro-gravity, for which a very accurate and robust description of the free surface is required[1,3,8–11]. By means of a local height function near the free surface, ComFLOW yields improved performance in terms of mass conservation and the number of disconnected droplets compared to the original VOF method[19]. Later, the methodology was extended to simulations of green water loading on a fixed deck[2,4,7], simulations of impact loads on fixed structures[2,4–7,11–14,18] and simulations of sloshing tanks[12–17].

### 3.1 Cell labeling method

Every grid cell is given a label to distinguish between fluid, air and boundary. These labels depend on the variables $F_b$ and $F_s$, which denote the fraction of a grid cell open for fluid and the fraction of a cell filled with the liquid phase, respectively. The interior cells containing no fluid, i.e. $F_b > 0$ and $F_s = 0$, are labeled as E(mpty) cells. Non-empty cells ($F_s > 0$) adjacent to E cells are labeled as S(urface) cells, as they must contain part of the free surface. All the remaining non-empty cells are labeled F(ull) cells. Cells satisfying $F_s = F_b = 0$ are called B(oundary) cells when they are adjacent to an interior cell, otherwise they are labeled as e(X)terior. In Figure 1, an example of a label configuration is shown. The labeling system stems from a one-phase model, but is retained in the current two-phase model. In one-phase simulations, E-cells are truly empty and are left out of the computations, while free surface boundary conditions are prescribed around S-cells. In the two-phase model, E-cells are filled with air and are thus included in the simulation.

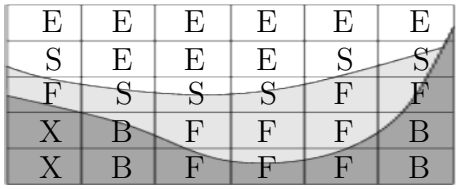


Figure 1: *Two dimensional grid-cell labeling for an arbitrary geometry and liquid configuration. Dark and light shading represent solid body and liquid, respectively.*

### 3.2 Discretisation of the Navier-Stokes equations

For presentational purposes, first-order Forward Euler time discretisation, with time levels $n$ and $n+1$ and time step $\Delta t$, is applied to equations (1) and (2),

$$\frac{\rho^{n+1}-\rho^n}{\Delta t} + \rho^n \nabla \cdot \vec{u}^{\,n+1} + \vec{u}^{\,n} \nabla \rho^n = 0 \tag{5}$$

$$\frac{\vec{u}^{\,n+1}-\vec{u}^{\,n}}{\Delta t} + \frac{\vec{u}^{\,n}}{\rho^n}\frac{\rho^{n+1}-\rho^n}{\Delta t} + \frac{1}{\rho^n}\nabla \cdot (\rho^n \vec{u}^{\,n} \vec{u}^{\,n}) + \frac{1}{\rho^n}\nabla p^{n+1}$$
$$-\frac{1}{\rho^n}\nabla\Big(\mu^n\left(\nabla \vec{u}^{\,n} + \nabla \vec{u}^{T\,n}\right) - \frac{2}{3}\mu^n \nabla \cdot \vec{u}^{\,n}\Big) - \vec{F}^n = 0, \tag{6}$$

Spatial discretisation is done on a staggered Cartesian grid, with the pressure located in cell centers and velocities in the middle of cell faces. The convective term $\frac{1}{\rho^n}\nabla\cdot(\rho^n \vec{u}^{\,n}\vec{u}^{\,n})$ in (6), which dominates in case of momentum-driven applications, is treated with symmetry preserving spatial discretisation[20]. With the first-order upwind (B2) scheme, artificial diffusion is applied to obtain stable solutions, leading to an abundant damping of fluid motion. Using the second-order upwind (B3) scheme, the level of artificial diffusion is much smaller, resulting in less damping. However, for B3 an alternative time discretisation is needed to obtain stable solutions, such as the second-order Adams-Bashforth (AB) method[1,8–11,13–18]. The combination of B3 (spatial-) with AB (time-)discretisation makes the numerical method ComFLOW second order accurate in both space and time.

Both time discretisation methods FE and AB are limited in their stability by the CFL number $\eta = u\Delta t/\Delta x$ and diffusion number $d = 2\mu\Delta t/(\Delta x)^2$. In most offshore cases, convection dominates diffusion, and in practice the CFL number $\eta$ controls the stability limit. For the combination B2 + FE, the CFL limit is $\eta_{max} \leq 1 - d \approx 1$. Unfortunately, for B3 + AB, this limit is somewhat lower $\eta_{max} \leq \frac{1}{4} - \frac{1}{2}d \approx \frac{1}{4}$, but as discussed above, it is needed to reduce artificial damping of fluid motion.

### 3.3 Solving the pressure

The pressure is calculated from a Poisson equation. Taking the divergence of (6) and substitution of the resulting term $\nabla \cdot \vec{u}^{\,n+1}$ into (5) leads to

$$\Delta t \nabla \cdot \left( \frac{1}{\rho^n} \nabla p^{n+1} \right) = \frac{1}{\rho^n} \frac{\rho^{n+1} - \rho^n}{\Delta t} + \frac{\vec{u}^n}{\rho^n} \cdot \nabla \rho^n + \nabla \cdot \tilde{\vec{u}}^n. \tag{7}$$

The term $\tilde{\vec{u}}$ denotes an 'intermediate' velocity, which includes convective, diffusive and force effects. The unknown term $\rho^{n+1}$ is reformulated through an equation of state. The treatment of this term, in combination with the density gradient term, requires more attention and has been described in[15,16,18]. The Poisson equation thus reduces to

$$\Delta t \nabla \cdot \left( \frac{1}{\rho^n} \nabla p^{n+1} \right) = \frac{F_b^n - F_s^n}{F_b^n \rho^n} \left( \frac{\rho_g^{n+1} - \rho_g^n}{\Delta t} + \vec{u}^n \nabla \rho_g^n \right) + \nabla \cdot \tilde{\vec{u}}^n. \tag{8}$$

The derivatives of the density in (8) no longer contain large jumps, as they are only determined by the compression and expansion of the gas phase. The gas density $\rho_g^{n+1}$ in (8) is substituted using the polytropic equation of state (3). Finally, the density is linearized by a Newton approximation to eliminate the exponent $1/\gamma$ and then transferred to the left-hand side of the Poisson equation[13–18].

The Poisson equation is solved with a Krylov subspace method, using incomplete LU preconditioning for acceleration. The entries in the Poisson matrix may differ up to a factor 1000, because of the density jumps in case of two-phase flow. This enhances the need for a powerful solver. For one-phase flow simulations, the pressure is solved with Successive Over Relaxation (SOR), where the optimal relaxation parameter is adjusted automatically during the iterations[21].

### 3.4 Free-Surface displacement

In principle, the motion of the free surface is described by (4). Numerically, the free surface displacement is done in two steps: first it is reconstructed and then it is advected to the new position. The reconstruction is done with Simple Linear Interface Calculation (SLIC), where the interface consists of line segments that are constructed parallel or perpendicular to the major flow axes[19]. A characteristic drawback of SLIC is the unphysical creation of disconnected droplets, resulting from errors in the reconstruction. Moreover, in the original VOF method values are rounded off at the end of the displacement algorithm ($0 \leq F_s \leq 1$), leading to significant losses in liquid mass.

To prevent from isolated droplets and mass losses, a local height function (LHF) has been introduced in ComFLOW[1–18]. The LHF is applied in a $3 \times 3(\times 3)$ block (in 2D or 3D) of cells surrounding a central S-cell. First, the orientation of the free surface is determined (horizontal or vertical), depending on $F_s$ values in the surrounding block of cells. Next, the horizontal or vertical height in each row or column is computed by summing the $F_s$ values (see Figure 2). Based on the LHF, fluid is transported from one cell (donor) to another (acceptor), depending on the magnitude of velocity, time step and grid sizes. The free-surface at the new time instant is then reconstructed by means of another LHF. Compared to the original VOF method[19], the LHF approach results in significantly less droplets and water loss[1,2,5–7,11–18].

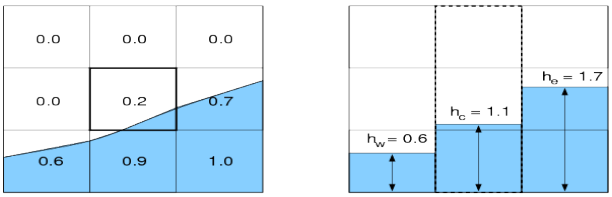


Figure 2: Construction of the local height function in a 3x3 block for a central S-cell.

An alternative method, which is however more difficult to implement, is proposed in[22]. Using this piecewise linear reconstruction method (PLIC), in 3D the interface is represented by oblique planes and the computational costs for the reconstruction of the free surface are strongly enhanced. Comparison learns that for certain flow applications slightly better results can be obtained[2]. However, for the wave-impact simulations considered in this study, the present LHF-method leads to satisfactory results.

### 3.5 Density at the free surface

Attention should be paid to the discretisation of the density $\rho$ in a cell, as it can vary up to factor of 1000. For compressible two-phase flow, $\rho$ in the cell center is given by

$$\rho = \frac{F_s}{F_b}\rho_l + \frac{(F_b - F_s)}{F_b}\rho_g, \tag{9}$$

where $\rho_g$ is a function of the pressure $p$ located in cell centers. Because of the staggered variable arrangement, $\rho$ is needed at cell edges as well. This a major point of attention, as spurious velocities may be generated when simple geometrical averaging is applied. By employing a so-called 'gravity-consistent' method, spurious velocities are avoided[13–17], as shown in Figure 3. This method is based on the observation that under hydrostatic conditions (no velocity), the momentum equation reduces to $\nabla p = \rho\vec{F}$. Since $\nabla\times\nabla = 0$, this gives $\nabla\times(\rho\vec{F} = 0)$, which provides a condition for the discrete average of $\rho$.

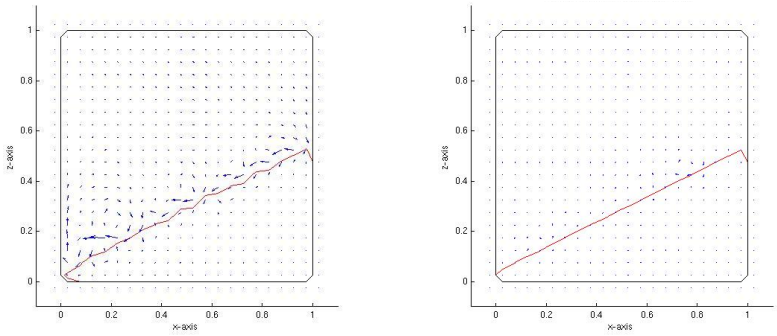


Figure 3: A hydrostatic case, with gravity perpendicular to the free surface. Spurious velocities are observed with simple geometrical density averaging (left). With gravity-consistent density averaging, the free surface stays at rest (right).

# 4 INCOMING AND OUTGOING WAVES

## 4.1 Wave generation

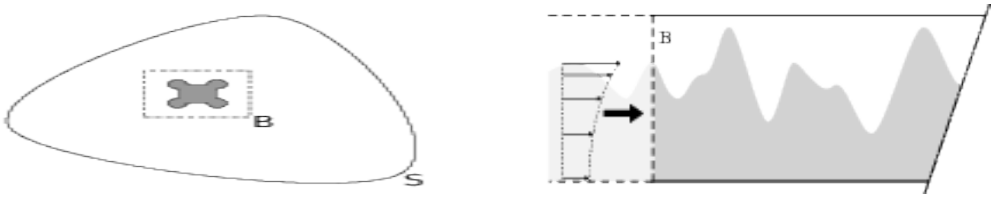


Figure 4: Left: the unbounded sea $S$ is truncated by an artificial near-field boundary $B$. Right: far-field wave behaviour determines the wave conditions at $B$.

For simulations of waves near offshore structures, the unbounded sea $S$ is truncated by an artificial near-field boundary $B$, see Figure 4. The size of the enclosed domain is preferably limited to the order of the length of the structure. Boundary $B$ should be fully open to flow, i.e. waves should flow into and/or leave the domain at $B$ without any disturbance. This is obtained by imposing boundary conditions that simulate wave behaviour. In case of regular waves, far-field wave behaviour can be modelled by analytical theory. For irregular waves, external numerical methods can be used that efficiently simulate wave propagation over long distances. Wave profiles obtained from far-field methods are then imposed as boundary condition on the near-field boundary, see Figure 4.

For steep long crested regular waves, often used in both experiments and numerical simulations, Rienecker and Fenton[23] (RF) formulated a system of non-linear equations, in which the combination of several harmonic base modes is fitted to both kinematic and dynamic free surface boundary conditions. The only approximation is the truncation of the number of base modes. Simulations have been performed to investigate how well these waves can be represented with ComFLOW. A very long 2D domain is used, which prevents reflected waves at the boundary from interfering with the results. Different grid resolutions were used, with 50, 100 and 200 cells per wave length and an aspect ratio $a = 1$. The surface elevations $\zeta$, obtained after 24 periods in the regular wave simulations, are presented in Figure 5. Non-linear effects are significant in steep waves in shallow water. Compared to the analytical (RF) solution, these waves can be simulated reasonably well when a large number of grid cells is used. In case of irregular waves, the longer components are represented quite well on comparable grids, but for shorter components significant mesh refinement is required[18].

## 4.2 Wave absorption

If they were known in advance, the far field wave kinematics could also be used for the absorption of outgoing waves. However, in our near-field simulations, there is always a structure inside the domain that diffracts and radiates waves away from the structure toward the domain boundaries, which cannot be anticipated in far-field computations.

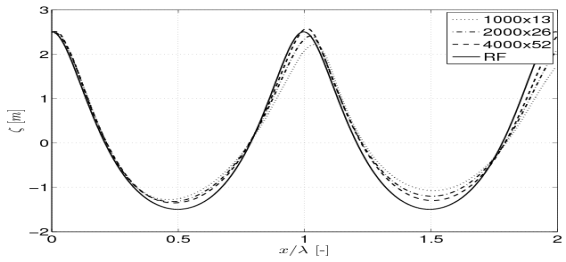


Figure 5: Free surface of a regular wave (period $T=6s$, height $H=4m$, length $\lambda\approx 50m$, water depth $d=10m$) at $t=144s$ (2 wave lengths). Simulations on different grids are compared to the analytical RF solution. Indicated grids cover the entire domain.

To prevent wave reflections, absorbing layers or dissipation zones can be employed, such as the pressure damping zone presented in[24]. An additional free surface pressure $p_s$ is used, proportional to the vertical velocity $w$ at the free surface, which counteracts wave motion. Its effect is increased slowly from the beginning of the dissipation zone toward the end of the domain, to prevent wave reflection from the dissipation zone itself

$$p_s = \alpha\left(x\right) w\left(x,t\right)|_{F_S}\,, \tag{10}$$

where $\alpha$ denotes the (variable) dissipation coefficient. In long waves, $w\approx 0$ and hence this pressure damping will not be very effective. In that case, large dissipation zones are required, which however significantly add to the domain size and hence to the computational effort. Therefore, we have developed an absorbing boundary condition (ABC) that gives less reflection, especially for long waves, but does not add to the domain size.

## 5 ABSORBING BOUNDARY CONDITION (ABC)

The Sommerfeld condition for the potential $\Phi$ is given by

$$\left(\frac{\partial}{\partial t} + c^{out}\frac{\partial}{\partial x}\right)\Phi^{out} = 0, \tag{11}$$

with $c^{out}$ the phase velocity of an outgoing wave component, propagating in positive $x$-direction. Condition (11) is perfectly absorbing for this single wave component, but gives reflections for wave components with other phase velocities. The level of reflection is measured by the reflection coefficient

$$R = \frac{c^{out} - c(kh)}{c^{out} + c(kh)}, \tag{12}$$

in which $c(kh)$ is the true phase velocity of the wave component arriving at the boundary.

The reflection of the ABC for all wave components can be reduced by one order of magnitude, when the condition is expanded to second order

$$\prod_{j=1}^{2}\left(\frac{\partial}{\partial t} + c_j\frac{\partial}{\partial x}\right)\Phi = 0. \tag{13}$$

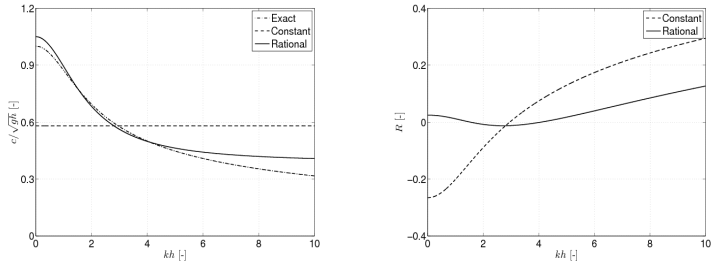


Figure 6: Two approximations of the dispersion relation (left) and their reflection coefficients (right).

The boundary condition operator now contains higher derivatives in time and in normal direction to the boundary. Spatial derivatives need to be implemented as one sided numerical operators, which may adversely affect the stability of the system[25]. Higher derivatives in time are also undesirable, because cells that were empty at one moment in time, may become filled during the next time step. In these cells, higher time derivatives cannot be resolved, because insufficient information from the past is available. Therefore, we follow an alternative approach, inspired by[26,27].

Consider the fact that the constant function $c = c^{out}$ is actually a poor approximation of the true (linear) dispersion relation, given by

$$c = \sqrt{gh}\sqrt{\frac{\tanh(kh)}{kh}}, \tag{14}$$

where $\sqrt{gh}$ is the shallow water phase velocity limit and $kh$ is the dimensionless wave number. Unfortunately, (14) cannot be substituted into (11), as it cannot be formulated in terms of differential operators. Therefore, the following rational approximation of the dispersion relation (14) is introduced

$$c_a \approx \sqrt{gh}\frac{a_0 + a_1(kh)^2}{1 + b_1(kh)^2}, \tag{15}$$

where the coefficients $a_0$, $a_1$ and $b_1$ are chosen such that (14) is approximated well over the largest possible range of $kh$-values. The Sommerfeld (constant) and rational function approximation of the dispersion relation (14) are shown in Figure 6(left).

Due to the exponential behaviour ($e^{-kz}$) of $\Phi$ in $z$-direction, the wave number in (15) can be replaced by second derivatives along the boundary: $k^2\Phi^{out} = \frac{\partial^2}{\partial z^2}\Phi^{out}$. Combination of (11) and (15) then yields the formulation of the ABC for dispersive waves

$$\left[\left(1+b_1h^2\frac{\partial^2}{\partial z^2}\right)\frac{\partial}{\partial t} + \sqrt{gh}\left(a_0+a_1h^2\frac{\partial^2}{\partial z^2}\right)\frac{\partial}{\partial x}\right]\Phi^{out}=0 \tag{16}$$

In Figure 6(right), the reflection coefficient of (16) is given for a range of wave components. Compared to the constant (Sommerfeld) approximation, the reflection coefficient of the rational approximation is smaller over a wide range of $kh$-values.

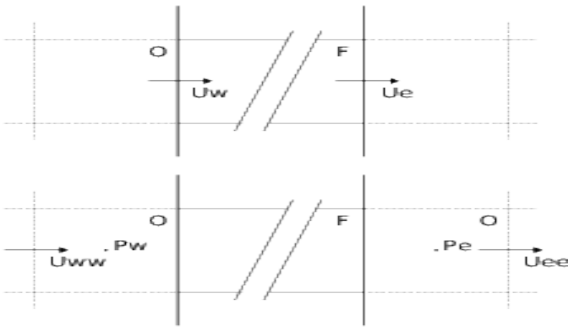


Figure 7: Top: boundaries at the left and right side coincide with $x$-locations of $u$. Bottom: for interpolation of $p$ exactly on the boundaries, mirror cells (labeled with O) are introduced containing $p_w$ and $p_e$.

### 5.1 Numerical implementation

In ComFLOW, the ABC (16) will be implemented at the boundary, which is chosen to coincide with the $x$-position of the horizontal velocity $u$ in a cell, see Figure 7. The time derivative of $\Phi$ in (16) is formally replaced by the pressure according to the linearized Bernoulli equation $\partial\Phi/\partial t = -p - gz$. The spatial derivative normal to the boundary is replaced by the horizontal velocity, i.e. $\partial\Phi/\partial x = u$. To prevent phase differences and resulting spurious reflections, $p$ in the ABC is evaluated exactly on the boundary, at the same $x$-position as $u$. As variables are staggered inside cells, interpolation of $p$ over the boundary is required and a mirror cell for the pressure is introduced, see Figure 7.

The velocity and pressure have to be evaluated at the same location, but also at the same instant $t^{n+1}$. The momentum equation is used to eliminate $u_{n+1}$

$$u_b^{n+1} = u_{i-1}^{n+1} = \tilde{u}_{i-1} - \frac{\Delta t}{\Delta x}\left(p_i - p_{i-1}\right)^{n+1}. \tag{17}$$

Note that $\tilde{u}$ contains the effect of convection and diffusion, as discussed above. Vertical derivatives in (16) are approximated by a numerical operator $\mathcal{V} = (\mathcal{V}_1, \mathcal{V}_2, \mathcal{V}_3)$ for the second derivative. For presentational purposes, vectors for $u$ and $p$ are introduced:

$$\vec{\tilde{u}} = \left(\tilde{u}_{k-1} \;\; \tilde{u}_k \;\; \tilde{u}_{k+1}\right)^T, \qquad \vec{p} = \left(p_{k-1} \;\; p_k \;\; p_{k+1}\right)^T \tag{18}$$

Combining (17) and (18) yields the discrete version of the ABC

$$\left(\mathcal{C}_{lz} \;\; \mathcal{C}_{xl} \;\; \mathcal{C}_{ln}\right)\vec{p}_{i-1} + \left(\mathcal{C}_{zl} \;\; \mathcal{C}_c \;\; \mathcal{C}_{zr}\right)\vec{p}_i = gz_p + \mathcal{R}\vec{\tilde{u}}_{i-1}. \tag{19}$$

In (19), the matrix coefficients $\mathcal{C}$ and right-hand side vector $\mathcal{R}$ are equal to:

$$\begin{array}{lllllllll}
\mathcal{C}_{lz} & = & (-\chi\tau + \frac{1}{2}\psi)\mathcal{V}_1 & \mathcal{C}_{xl} & = & -\varphi\tau + \frac{1}{2} - (\chi\tau - \frac{1}{2}\psi)\mathcal{V}_2 & \mathcal{C}_{ln} & = & (-\chi\tau + \frac{1}{2}\psi)\mathcal{V}_3 \\
\mathcal{C}_{zl} & = & (\chi\tau + \frac{1}{2}\psi)\mathcal{V}_1 & \mathcal{C}_c & = & \varphi\tau + \frac{1}{2} + (\chi\tau + \frac{1}{2}\psi)\mathcal{V}_2 & \mathcal{C}_{zr} & = & (\chi\tau + \frac{1}{2}\psi)\mathcal{V}_3
\end{array}$$

$\mathcal{R} = (\chi\mathcal{V}_1 \quad \varphi - \chi\mathcal{V}_2 \quad \chi\mathcal{V}_3)$,

with $\varphi = \sqrt{gh}a_0$, $\chi = \sqrt{gh}a_1h^2$, $\psi = b_1h^2$ and $\tau = \Delta t/\Delta x$.

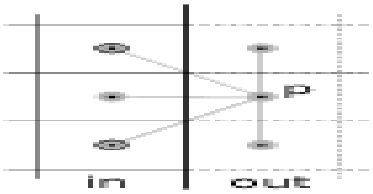


Figure 8: Pressure stencil at the boundary to determine $p$ from the ABC.

The discrete ABC (19) is essentially an equation for $p$ in a mirror cell outside the domain. On the left-hand side, it only features pressures at the new time level $t^{n+1}$. The other side has horizontal velocities at time level $t^n$, stemming from convective and diffusive terms. In Figure 8, the stencil of pressures is shown for the discrete boundary condition operator and the position of the matrix coefficients in (19). The structure of the discrete ABC bears great resemblance to the pressure Poisson equation (8) and can therefore easily be combined with the field equations for the inside of the domain.

### 5.2 Numerical performance

The performance of the ABC can be investigated by comparing the free surface at a specific position in two simulations with different domains. A very long domain is considered, where the surface elevation at the measurement position ($x_m = 200m$) cannot be disturbed by reflections, and a much shorter domain (length $400m$) with ABC at the boundary, see Figure 9(left). The grid resolution is $\Delta x \times \Delta z = 1m \times 0.5m$, with 5% vertical stretching. An ensemble of irregular waves (wave height $H_s = 4m$, peak period $T_p = 15s$, water depth $d = 100m$) is simulated during $600s$. The imposed and simulated spectra at the measurement position $x_m$ are shown in Figure 9(right). Everything but the boundary condition being the same, any difference can only be attributed to reflection of the ABC.

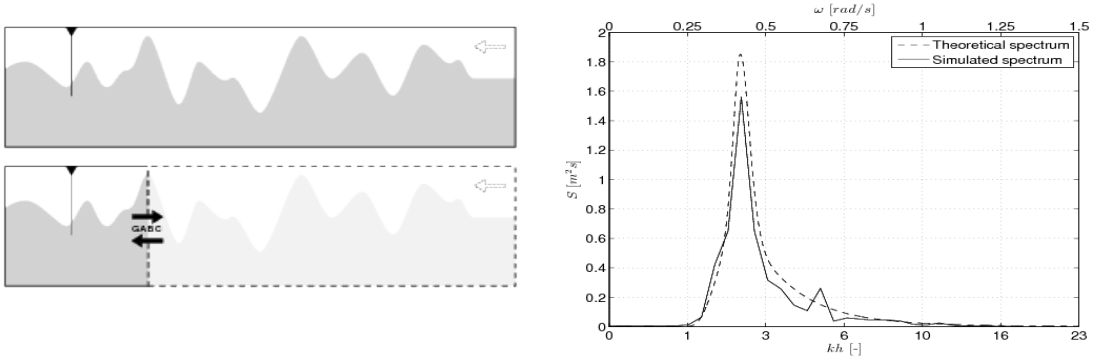


Figure 9: Left: a long domain and a short domain with ABC. Surface elevations at the indicated position determine reflections. Right: theoretical and simulated spectrum at the measurement position ($x_m = 200m$).

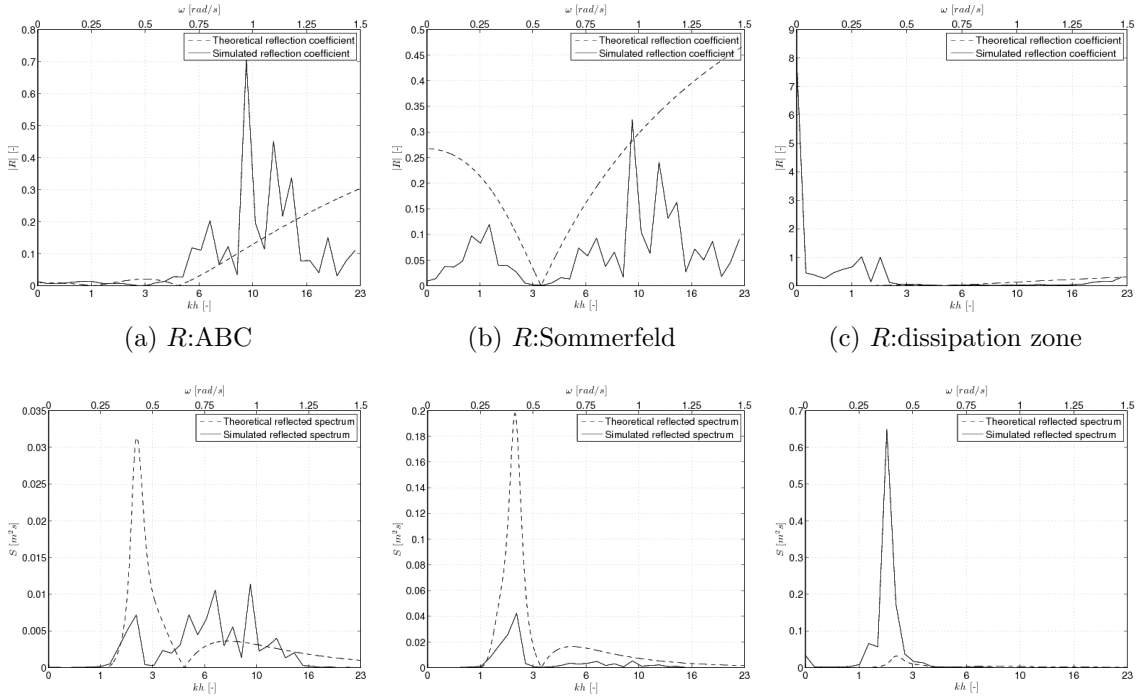


(a) $R$:ABC (b) $R$:Sommerfeld (c) $R$:dissipation zone

(d) $S$:ABC (e) $S$:Sommerfeld (f) $S$:dissipation zone

Figure 10: The reflection coefficients $R$ (a,b,c) and spectra $S$ (d,e,f) obtained with ABC, Sommerfeld and dissipation zone.

Time traces for the reflected waves are obtained by subtracting the surface elevation at $x_m$ in the long domain, from that at $x_m$ in the short domain. These time traces are converted to reflection spectra and reflection coefficients, as shown in Figure 10(a-d). The ABC has been compared to the theoretical reflection coefficient (12) and to the reflection coefficient of the Sommerfeld equation. The performance of the ABC is generally better than the Sommerfeld condition and accords well with theory. The results do seem to show that the ABC does not perform well for the shorter components, but please note that these components are not represented well on the grid. Moreover, very little wave energy resides at these frequencies, which may adversely influence the results.

The simulation with ABC has also been compared to a simulation with a pressure damping zone, with dissipation coefficient $\alpha = 0.05$ in (10). The domain was chosen 3 times as long as the domain with ABC ($3 \times 400 = 1200m$). The theoretical reflection for this configuration is 2% for wave components near the peak frequency of the spectrum. The numerically obtained reflection was 100%. Hence, the dissipation zone is not very well suited for these wave components. The results in Figure 10(e-f) also show that very long wave components are generated due to non-linear effects in the dissipation zone.

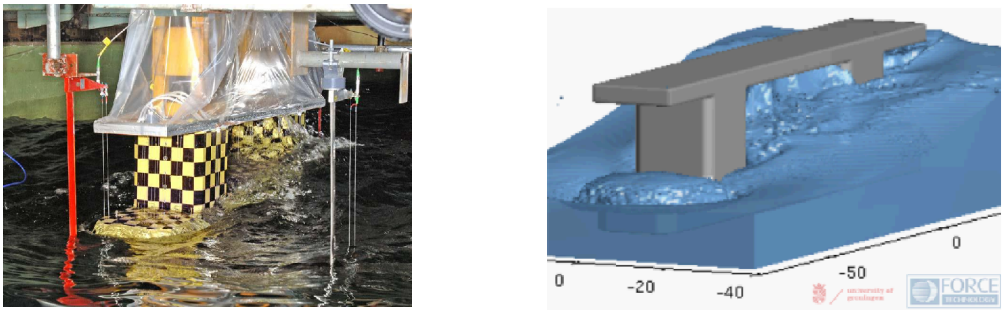


Figure 11: The semi-submersible model in the experiments and a snapshot of a simulation of the wave run-up against the two columns.

## 6 VALIDATED RESULTS

The performance of the ABC has been tested for waves around a model of an offshore structure. The 1:50 simplified model of the semi-submersible consists of two columns and a pontoon under water, see Figure 11. At full scale, the pontoon measures $l \times w \times h = 114.5m \times 17.5m \times 10m$. The column width is $17.5m$ and they are $43.5m$ apart. The total draft is $16m$ and the air gap $12m$. The model was kept restrained, to give the largest level of diffraction and run-up of water on the columns. Deck impacts are almost guaranteed, which is highly undesirable for an actual design, but gives the best circumstances for validation of the numerical model. The experiments were performed in a very long, but quite narrow wave basin of $180m$ deep. Waves were generated with a wave board at one of the narrow ends. At the opposing end a beach induced wave breaking and prevented reflection. The model was placed at considerable distance behind the wave board.

Figure 12: Positions of the sensors for surface elevation (left) and pressure (right).

During the experiments, surface elevations were measured around and in between columns and at some distance away from the structure. The columns and the deck were equipped with pressure transducers to monitor the build-up of pressure during a wave impact. In Figure 12, the positions of the pressure and wave-height sensors are shown. Several sea states were created: regular long crested waves of different periods and wave heights, as well as a number of irregular long crested waves.

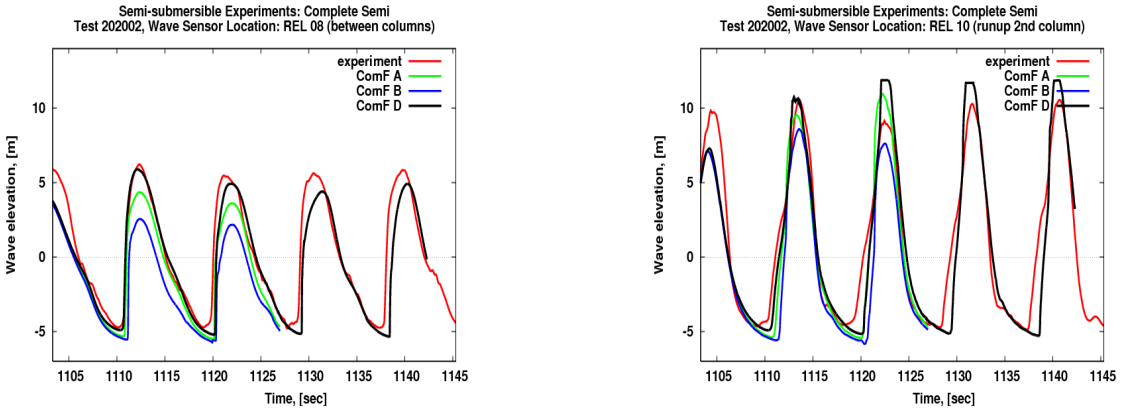


Figure 13: Wave height between the columns (left) and run-up on the 2nd column (right).

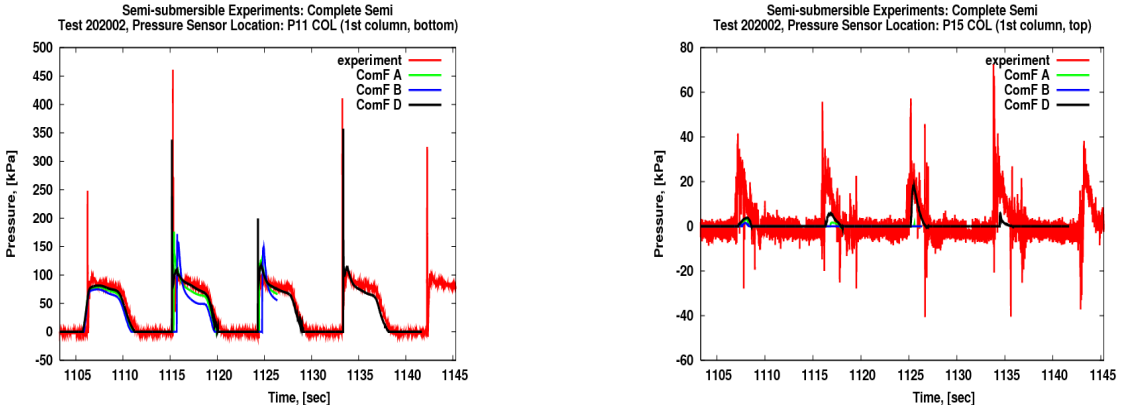


Figure 14: Pressure on the first column, near the pontoon (left) and near the deck (right).

A regular wave experiment ($H = 15m$ and $T = 11s$) is considered below. For computational efficiency, the domain has to be truncated to the direct surroundings of the structure. The upstream and downstream boundaries of the computational domain are located half a (significant) wave length in front and behind the structure. The incoming waves are modeled with 5th order Stokes potential theory and have been calibrated to establish a representative incoming wave. In accordance with the experiment, the side walls of the domain are fully reflecting and positioned at the location of the side wall of the basin ($y = -100m$ and $y = 100m$). At the inflow and outflow boundaries, ABCs are used to absorb outgoing waves.

The simulations have been performed with two different water depths. In cases A and B the water depth was half of the true depth ($0.5 * 180 = 90m$) to save computation time, whereas case D is a simulation with full depth. Different uniform grid resolutions were used for the different cases: $\Delta x, y, z = 0.8m$ (case A) and $\Delta x, y, z = 0.5m$ (cases B and D). The results of the simulations are compared to measured signals. In Figure 13, the wave heights between the columns and the run-up on the 2nd column of the semi-submersible

are shown. In Figure 14, the pressure at two locations on the first column are shown: one near the pontoon and the other near the deck. In case of the best grid resolution, the agreement with the experiment is generally good. The surface elevation near the columns is well represented and the pressure on the upstream column near the pontoon is very close to the measured pressure. The pressure near the deck is underpredicted, which can be attributed to the limited number of grid cells along the column.

## 7 CONCLUSION

The numerical method ComFLOW is suitable for the simulation of two-phase flow in extreme wave impact events, where the free surface may assume any shape. The method can accurately simulate the propagation of both regular and irregular waves, although the required grid resolution is quite demanding.

The numerical method has been combined with a novel Absorbing Boundary Condition (ABC) for long crested dispersive waves. The boundary condition consists of the Sommerfeld condition, combined with a rational approximation of the true linear dispersion relation and vertical derivatives along the boundary.

In numerical simulations of irregular waves, the ABC performs in accordance with the theoretical reflection coefficient. For irregular waves, it gives less reflection than the Sommerfeld condition and also less reflection than a traditional dissipation zone, which was three times longer than the domain with ABC. In comparison with the dissipation zone, we have obtained less reflection, in combination with a reduction of the computational effort of roughly a factor four.

The ABC has been applied in 3D numerical simulations of wave impacts on a semi-submersible model. Surface elevations close to and pressures on the semi-submersible have been compared to experimental results. The overall agreement between simulations and experiments is good. Near the deck, the impact pressure is slightly underpredicted, which can probably be improved by means of grid refinement near the structure.

### Acknowledgment

This research is supported by the Dutch Technology Foundation STW, applied science division of NWO and the technology programme of the Ministry of Economic Affairs (#06433). We thank the Maritime Research Institute Netherlands (MARIN) for the experimental results and FORCE Technology Norway for processing the simulation data.

## REFERENCES

[1] A.E.P. Veldman, J. Gerrits, R. Luppes, J.A. Helder and J.P.B. Vreeburg, The Numerical Simulation of Liquid Sloshing On Board Spacecraft. *J. Comp. Phys.*, **224**:82–99, (2007).

[2] K.M.T. Kleefsman, G. Fekken, A.E.P. Veldman, B. Iwanowski and B. Buchner, A Volume-Of-Fluid Based Simulation Method for Wave Impact Problems. *J. Comp.*

*Phys.*, **206(1)**:363–393, (2005).

[3] J. Gerrits and A.E.P. Veldman, Dynamics of Liquid-Filled Spacecraft. *J. Eng. Math.*, **45**:21–38, (2003).

[4] K.M.T. Kleefsman, G. Fekken, A.E.P. Veldman, B. Buchner, T. Bunnik and B. Iwanowski, Prediction of green water and wave loading using a Navier-Stokes based simulation tool. In *21st Int. Conf.*, (2002). OMAE2002-28480.

[5] K.M.T. Kleefsman and A.E.P. Veldman, An improved Volume-Of-Fluid method for wave impact. In *4th Eur. Congr.* ECCOMAS, (2004).

[6] K.M.T. Kleefsman, A.E.P. Veldman and T. Bunnik, An improved Volume-Of-Fluid (IVOF) method for wave impact type problems. In *Spec. Symp. on FPSO Integrity*, (2004). OMAE-FPSO04-0066.

[7] K.M.T. Kleefsman, G.E. Loots, A.E.P. Veldman, B. Buchner, T. Bunnik and E. Falkenberg, The numerical solution of green water loading including vessel motions and the incoming wave field. In *24th Int. Conf.*, (2005). OMAE2005-67448.

[8] R. Luppes, J.A. Helder and A.E.P. Veldman, Liquid sloshing in microgravity. In *56th Int. Astr. Congr.* IAF, (2005). IAF-05-A2.2.07.

[9] R. Luppes, J.A. Helder and A.E.P. Veldman, The numerical simulation of liquid sloshing in microgravity. In *Eur. Conf.* ECCOMAS CFD, (2006). ISBN 909020970-0, paper490.

[10] R. Luppes, J.A. Helder and A.E.P. Veldman, The numerical simulation of liquid sloshing in microgravity. In *Computational Fluid Dynamics 2006*, pages 607–612. ICCFD, (2009). doi: 10.1007/978-3-540-92779-2-95.

[11] A.E.P. Veldman The simulation of violent free-surface dynamics at sea and in space. In *Eur. Conf.* ECCOMAS CFD, (2006). ISBN 909020970-0, paper 492.

[12] R. Wemmenhove, G.E. Loots, R. Luppes and A.E.P. Veldman Modeling two-phase flow with offshore applications. In *24th Int. Conf.*, (2005). OMAE2005-67460.

[13] R. Wemmenhove, G.E. Loots and A.E.P. Veldman, Numerical simulation of hydrodynamic wave loading by a two-phase model. In *Eur. Conf.* ECCOMAS CFD, (2006). ISBN 909020970-0, paper 517.

[14] R. Wemmenhove, G.E. Loots and A.E.P. Veldman, Hydrodynamic wave loading on offshore structures simulated by a two-phase flow model. In *25th Int. Conf.*, (2006). OMAE2006-92253.

[15] R. Wemmenhove, R. Luppes, A.E.P. Veldman and T. Bunnik Numerical Simulation of Sloshing in LNG Tanks with a Compressible Two-Phase Model. In *26th Int. Conf.*, (2007). OMAE2007-29294.

[16] R. Wemmenhove, R. Luppes, A.E.P. Veldman and T. Bunnik Application of a VOF Method to Model Compressible Two-Phase Flow in Sloshing Tanks. In *27th Int. Conf.*, (2008). OMAE2008-57254.

[17] R. Luppes, R. Wemmenhove, A.E.P. Veldman and T. Bunnik Compressible Two-Phase Flow in Sloshing Tanks. In *5th Eur. Congr.* ECCOMAS, (2008).

[18] P.R. Wellens, R. Luppes, A.E.P. Veldman and M.J.A Borsboom. CFD simulations of a semi-submersible with absorbing boundary conditions. In *28th Int. Conf.*, (2009). OMAE2009-79342.

[19] C.R. Hirt and B.D. Nichols, Volume Of Fluid (VOF) Method for the Dynamics of Free Boundaries. *J. Comp. Phys.*, **39**:201–225, (1981).

[20] R.W.C.P. Verstappen and A.E.P. Veldman, Symmetry-Preserving Discretisation of Turbulent Flow. *J. Comp. Phys.*, **187**:343–368, (2003).

[21] E.F.F. Botta and M.H.M. Ellenbroek, A modified SOR method for the Poisson equation in unsteady free-surface flow calculations. *J. Comp. Phys.*, **60**:119–134, (1985).

[22] D.L. Youngs, Time-dependent multi-material flow with large fluid distortion. In K. W. Morton and M. J. Baine, editors, *Numerical Methods for Fluid Dynamics*, pages 273–285. Academic Press, New York, (1982).

[23] M.M. Rienecker and J.D. Fenton, A Fourier Approximation Method for Steady Water-Waves. *J. Fluid Mech.*, **104**:119–137, (1981).

[24] J.H. Westhuis, Approximate analytic solutions and numerical wave tank results for the reflection coefficients of a class of numerical beaches. In *10th Int. Conf.*, pages 245–252. ISOPE, (2000).

[25] D. Givoli and B. Neta, High-Order Nonreflecting Boundary Conditions for the Dispersive Shallow Water Equations. *J. Comput. and Appl. Math.*, **158**(1):49–60, (2003).

[26] B. Engquist and A. Majda, Absorbing Boundary-Conditions for Numerical-Simulation of Waves. *Math. of Comput.*, **31**:629–651, (1977).

[27] K. Dgaygui and P. Joly, Absorbing Boundary-Conditions for Linear Gravity-Waves. *Siam J. Appl. Math.*, **54**(1):93–131, (1994).